JGR Atmospheres

RESEARCH ARTICLE
10.1029/2022JD037466

Evolution and Features of Dust Devil-Like Vortices in Turbulent Rayleigh-Bénard Convection—An Experimental Study

Christian Kaestner[1], Julien David Schneider[1], and Ronald du Puits[1]

[1]Institute of Thermodynamics and Fluid Mechanics, Technische Universitaet Ilmenau, Ilmenau, Germany

Key Points:

- Dust devil-like vortices spontaneously evolve in turbulent Rayleigh-Bénard convection at sufficiently high Rayleigh numbers $Ra > 10^{10}$
- We studied their properties in a large-scale Rayleigh-Bénard experiment using Lagrangian particle tracking velocimetry
- The vortical structures in the laboratory experiment are weaker than atmospheric dust devils, but they exhibit similar features

Correspondence to:

C. Kaestner,
christian.kaestner@tu-ilmenau.de

Citation:

Kaestner, C., Schneider, J. D., & du Puits, R. (2023). Evolution and features of dust devil-like vortices in turbulent Rayleigh-Bénard convection—An experimental study. *Journal of Geophysical Research: Atmospheres*, *128*, e2022JD037466. https://doi.org/10.1029/2022JD037466

Received 8 JUL 2022
Accepted 4 JAN 2023

Author Contributions:

Conceptualization: Christian Kaestner
Data curation: Christian Kaestner
Formal analysis: Julien David Schneider
Funding acquisition: Ronald du Puits
Investigation: Julien David Schneider
Methodology: Christian Kaestner
Project Administration: Ronald du Puits
Resources: Ronald du Puits
Software: Julien David Schneider
Supervision: Ronald du Puits
Validation: Julien David Schneider
Visualization: Julien David Schneider
Writing – original draft: Christian Kaestner
Writing – review & editing: Julien David Schneider, Ronald du Puits

Abstract We present an experimental study simulating atmospheric dust devils in a controlled laboratory experiment. The experimental facility, called the "Barrel of Ilmenau" (www.ilmenauer-fass.de) represents a classical Rayleigh-Bénard set-up and is believed to model the phenomena in a convective atmospheric boundary layer fairly well. Our work complements and extends the numerical work of Giersch and Raasch (2021)https://doi.org/10.1029/2020jd034334 by experiments. Dust devils are thermal convective vortices with a vertical axis of rotation visualized by entrained soil particles. They evolve in the convective atmospheric boundary layer and are believed to substantially contribute to the aerosol transport into the atmosphere. Thus, their evolution, size, lifetime, and frequency of occurrence are of particular research interest. Extensive experimental studies have been conducted by field measurements and laboratory experiments so far. Beyond that, our study is the first attempt of Rayleigh-Bénard convection (RBC) in air to investigate dust devil-like vortices in a laboratory experiment. Up to now, this set-up mimics the natural process of dust devil evolution as closest to reality. The flow measurement was carried out by particle tracking velocimetry using neutrally buoyant soap bubbles. We initially identified dust devil-like vortices by eye from the Lagrangian velocity field, and in a later, more sophisticated analysis by a specific algorithm from the corresponding Eulerian velocity field. We analyzed their frequency of occurrence, observation time, and size. With our work, we could demonstrate that turbulent RBC is an appropriate model to mimic the natural process of the evolution of dust devils in the convective atmospheric boundary layer without artificial stimulation.

Plain Language Summary We could experimentally demonstrate that dust devil-like vortices spontaneously arise in turbulent Rayleigh-Bénard convection. This first-time experimental survey simulates the evolution of dust devil-like vortices in a laboratory experiment which mimics the convective atmospheric boundary layer quite closely and gets by without any artificial input of rotation. Dust devil-like vortices are measured and identified using the particle tracking velocimetry technique. Within an observation period of 2 hr, 56 dust devil-like vortices could be detected in total. Their properties coincide quite well with those structures identified in very recent direct numerical simulations (DNS) by Giersch and Raasch (2021, https://doi.org/10.1029/2020jd034334). As well, they show similarity to atmospheric dust devils. The size of our experimentally generated dust devil-like vortices starts at about 1 dm and ranges up to about 1 m. This is larger than in DNS, but still smaller than in the atmosphere or in large eddy simulation.

1. Introduction

Dust devils are micro-beta scale (20–200 m in horizontal scale; Stull, 1988), convective vortex structures with vertical rotational axis appearing at ground level of the atmosphere. They are detected in terrestrial and Martian atmospheres (Balme & Greeley, 2006). Dust devils occur, when hot air near a solar heated surface hotspot rises quickly through the cooler air layer above. The thermal convective phenomenon is initiated by "superadiabatic lapse rate" (Balme & Greeley, 2006) at the irradiated surface and continues as plume outside the thermal boundary layer (Sinclair, 1969). Under certain conditions, for example, local vortices initiated by convection or deflected wind at obstacles, the up-drafting air starts to rotate (Balme & Greeley, 2006; Carroll & Ryan, 1970; Renno et al., 2004). Due to vertical stretching of the uprising column of hot air, entrained dust moves toward the axis of rotation. Thus, conservation of angular momentum leads to increased tangential velocity at smaller radii, and hence, an enhancement of the spinning effect. A secondary flow induced by the pressure drop further sucks hot air horizontally from the surface inward to the bottom of the initial vortex structure (Metzger, 1999). Thus, the spinning effect continuously intensifies as more hot air rushes and raises and the vortex becomes

self-sustaining and forms a fully developed dust devil (Sinclair, 1969, 1973). Thus, a fully developed dust devil appears as a funnel-like chimney (columnar, V-shaped or just disordered, rotating dust cloud) in which air circulates and moves upwards (Metzger, 1999). During the uprising process, the hot air cools down and buoyancy decreases until air stops to rise. The rising hot air inside the vortex core displaces cool air descending at the outside of the vortex core. Dust devils frequently tilt with height (up to 10° or more [Kaimal & Businger, 1970; McGinnigle, 1966; Sinclair, 1973]) in the direction of their forward motion owing to surface friction. Continuing maintenance or even strengthening of the dust devil, may be gained by passing further surface hotspots. The size of dust devils ranges from a few meters up to over 1 km in height (Balme & Greeley, 2006; Murphy et al., 2016). They are usually at least five times higher than wide, with wind speeds of up to 25 m/s (Bell, 1967; Flower, 1936; G. D. Hess & Spillane, 1990; Sinclair, 1965; Williams, 1948). Their lifetime ranges from only a few minutes up to several hours (Idso, 1974; Mattsson et al., 1993; Metzger, 1999), whereby lifetime correlates with height as 1 hr for each 300 m of height (Ives, 1947). Beneficial for the formation of dust devils are arid, hot, flat surfaces with gentle slope and regions with strong horizontal thermal gradients (Brooks, 1960; Mattsson et al., 1993; Sinclair, 1969). The frequency of occurrence is inversely related to their size (Carroll & Ryan, 1970). Moreover, there is no preferred direction of rotation which indicates that their size is too small to be affected by Coriolis force (Carroll & Ryan, 1970; Morton, 1966; Sinclair, 1965).

A lot of experimental effort has been spent to investigate dust devils in their natural environment. Originally, dust devils were visually observed, obtaining statistics of features, motion, and frequency. Additionally, sensors like anemometers, pressure gauges, and temperature probes allowed to investigate the inner structure and composition of a dust devil. Within the pioneering work of Sinclair (1969), sensor arrays were pushed into the vortex to characterize the inner structure of a dust devil. Other authors report that they applied drones to fly the instrumentation inside the dust devil (Jackson et al., 2018), placed stationary sensors at the ground (Lorenz et al., 2015), or used LIDAR (light detection and ranging; Chan & Li, 2021) or Doppler radar (Bluestein et al., 2004) to investigate dust devils. Anyhow, stationary probes only provide useable data when a dust devil passes the sensors by chance. Besides LIDAR and radar, other non-invasive, contactless measurement techniques, for example, optical or spectroscopic methods, are limited in application since the dust devils are almost opaque. However, this is the only option to sustain the vortex against the measurement process itself due to physical interaction between sensor and flow. In general, field studies are often time consuming and require comprehensive technical equipment. They can interfere with the flow structure of the dust devils and do not allow continuous in situ sensing during the dust devil lifetime.

Thus, there is certain interest to perform laboratory experiments. Several studies were conducted to mimic the evolution of a dust devil in a laboratory experiment. First attempts were rotating hot plates, applying constant rotational momentum to a convective updraft (Barcilon, 1967; Fitzjarrald, 1973). These studies lacked accurate experimental parameters and the flow was often just laminar, that is, it was widely incomparable with the specifications of the atmosphere. Another way was to apply fans to generate a rotating channelized flow which was supposed to apply more realistic experimental parameters (Maxworthy, 1972; Mullen & Maxworthy, 1977). A great advancement and a more sophisticated way of mechanical evolution of dust devil-like vortices was the Arizona State University vortex generator (ASUVG) allowing the study of particle entrainment in more detail (Balme et al., 2001; Greeley et al., 2003; Neakrase & Greeley, 2010). Nevertheless, even this laboratory device is not fully capable of modeling the original process of dust devil evolution exclusively driven by natural thermal convection. Ringrose (2005) presented an approach somewhat closer to the natural environment. In this work, a heated metal plate surrounded by a vertical wall of pivotable Perspex windows was used. Such a set-up is known as Bénard convection (Bénard, 1901). But, due to the chimney-like structure of this convection cell, this experimentally prescribed amplification does also not represent the conditions in the real atmosphere very well. Nevertheless, dust devil-like vortices could already be observed in Rayleigh-Bénard convection (RBC), but only in water as working fluid (Willis & Deardorff, 1979).

Complementary numerical studies are almost all based on large-eddy simulations (LES) which reduce computational time at larger domains compared to direct numerical simulations (DNS; Giersch et al., 2019; Kanak, 2005). Since dust devils are only micro-beta scale structures compared to the entire atmospheric boundary layer, the spatial resolution of LES is often not sufficiently good (only a few meters) to resolve the inner structure of a dust devil. Thus, it is quite difficult to scale the LES that the cellular pattern of the boundary layer is well-represented and the dust devil structure is adequately resolved at once (Spiga et al., 2016). In particular, the surface layer as source of dust devils is inadequately resolved by sub-grid scale models (Ohno & Takemi, 2010; Raasch &

Franke, 2011; Sorbjan, 1996; Spiga et al., 2016; Sullivan et al., 1994). A further deficit of LES exhibits considering the potential kind of the formation of dust devils. They are believed to appear at the updraft intersection of two or more large-scale atmospheric convection rolls. Whilst LES is able to resolve such large convection rolls nicely, the local fluctuations and small vortices which possibly initiate the rotation of up-drafting hot air in the surface layer cannot be resolved. In order to overcome this problem, DNS which are able to resolve the flow field down to the smallest vortices would help. There is some related work on RBC, but with increasing size of the computational domain and the period to be simulated, the computational effort quickly increases beyond the actual capabilities (Cortese & Balachandar, 1993; Fiedler & Kanak, 2001; Giersch & Raasch, 2021).

In our study, we present a new experimental approach to generate dust devil-like vortices under more realistic boundary and initial conditions. We use turbulent RBC at a width-to-height ratio of 3 to mimic the conditions of the convective atmospheric boundary layer and to study potentially occurring vortex phenomena of the lower atmosphere, even though the Rayleigh number of the experiments is much lower than in atmosphere. Fodor et al. (2019) demonstrated that RBC is suitable to model the convective atmospheric boundary layer, at least in DNS. Giersch and Raasch (2021) conducted DNS under the same top and bottom boundary and initial conditions as applied in this experimental study and could finally detect dust devil-like vortices in their simulations. Our experiments complement these numerical simulations. The particular benefit of our measurements is the much longer observation period which is about 1,000 times longer than the simulation time (Exp.: 22 hr in total (2 hr evaluated in detail) versus DNS: 70 s). The extended measuring time improves the statistics for larger and thus rarer dust devil-like vortices, whose probability of occurrence decreases with growing size and who may not occur in DNS on short simulation times. Our experiments eventually complement the numerical results by expanding the range of detected structure size, but also contribute to validate the DNS (Giersch & Raasch, 2021) and LES (Giersch et al., 2019) models by generating a comparative database.

2. Methodology

2.1. Concept

To simulate the evolution of dust devil-like vortices close to their natural origin in the convective boundary layer of the Earth's atmosphere, experiments were conducted in a large-scale Rayleigh-Bénard cell called “Barrel of Ilmenau” (du Puits et al., 2007; Thess et al., 2001). This is an idealized experimental set-up to study natural thermal convection, but it also allows air flow studies in room ventilation (Lobutova et al., 2010). RBC is a canonical well-known set-up, which consists of a fluid layer uniformly heated from below, uniformly cooled from above and obeys adiabatic sidewalls. Similar to the convective atmospheric boundary layer, temperature decreases with increasing height above the bottom surface and the vertical extent of the fluid layer is set to be three times smaller than the horizontal one. Furthermore, due to the fact that condensation and radiation show only minor effects on the evolution of dust devils whereas thermal convection is the predominant driving force, we consider RBC as a very good experimental model to study dust devils.

The Rayleigh-Bénard set-up is characterized totally by five dimensionless numbers (Lienhard & John, 2005). The degree of turbulence is described by the Rayleigh number Ra and can be regarded as the ratio between buoyant and viscous forces:

$$Ra = \frac{g\beta(T_h - T_c)L^3}{\nu\kappa}. \tag{1}$$

The Prandtl number Pr depicts the ratio between kinematic viscosity and thermal diffusivity:

$$Pr = \frac{\nu}{\kappa} = \frac{\eta}{\rho\kappa}. \tag{2}$$

The Reynolds number Re describes the ratio between inertial and viscous forces:

$$Re = \frac{uL}{\nu} = \frac{\rho uL}{\eta}. \tag{3}$$

The Nusselt number Nu is the ratio of convective and conductive heat transfer:

$$Nu = \frac{hL}{\lambda}. \tag{4}$$

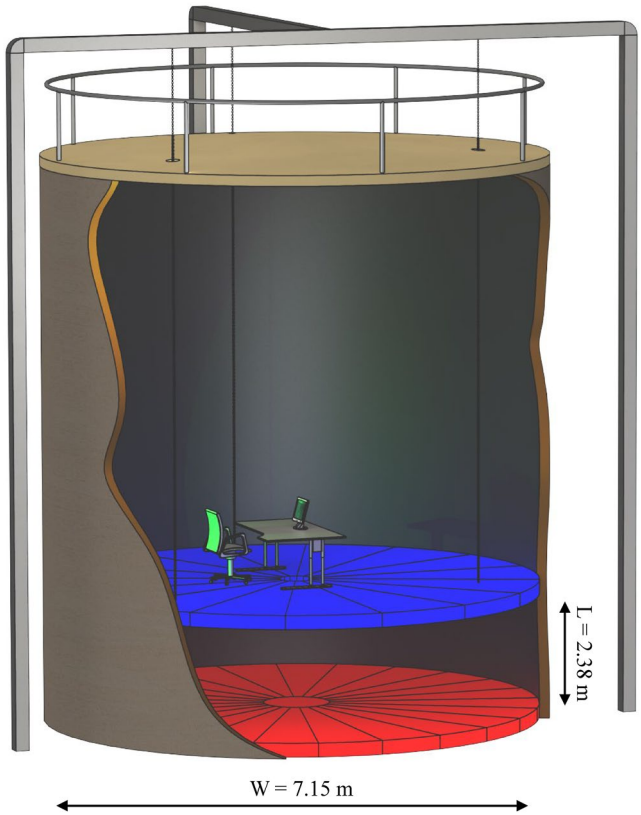

Figure 1. Schematic of the "Barrel of Ilmenau".

In these definitions, ρ is the density of the fluid, ν the kinematic viscosity, η the dynamic viscosity, u the velocity, κ the thermal diffusivity, g the acceleration due to gravity, β the thermal expansion coefficient, λ the thermal conductivity, h the convective heat transfer coefficient, L the characteristic linear dimension in vertical direction, T_h the surface temperature of the hot plate and T_c the surface temperature of the cold plate. A further dimensionless number, characterizing the ratio of the horizontal extent W and the vertical extent L of the convection cell is the aspect ratio Γ:

$$\Gamma = \frac{W}{L}. \tag{5}$$

Our Rayleigh-Bénard cell has a cylindrical shape with a diameter $W = 7.15$ m and a height $L = 2.38$ m resulting in an aspect ratio $\Gamma = 3$. A schematic of the "Barrel of Ilmenau" is shown in Figure 1. The large size of the convection experiment ($V = 95.6$ m^3) allows to set a turbulent flow in this specific geometry with Rayleigh numbers up to $Ra = 5 \times 10^{10}$. It furthermore enables the reproduction of large-scale convective flow structures which can be measured using optical measurement techniques. In our experiments, we set the temperatures of the bottom and top plates to values that correspond to Rayleigh numbers $Ra = 1.3 \times 10^{10}$ and $Ra = 2.5 \times 10^{10}$, respectively. Even though, this is far from the Rayleigh number of the atmospheric boundary layer with $Ra \approx 10^{18}$, the simulations by Giersch and Raasch (2021) confirmed Rayleigh numbers $Ra \approx 10^{10}$ to be sufficiently high to generate dust devil-like vortices. However, Giersch and Raasch (2021) applied 10°C and 50°C to the upper and lower plate, respectively, whereas in our experiments the temperatures were set to 20°C/15°C and 30°C/25°C for set-up I (HS/no.HS) and 15°C and 35°C for set-up II (HS and no.HS; compare Table 1, Figure 3), respectively. Nevertheless, the Rayleigh numbers are of the same order of magnitude and so far well-comparable. The Prandtl number was $Pr = 0.71$ for air as working fluid. The wall was equipped with a thermal shield to maintain adiabatic boundary conditions (Du Puits et al., 2013). We applied four different settings to study the evolution of dust devil-like vortices in turbulent RBC. In a first set-up, we measured the flow almost in the entire fluid volume. This measurement serves to evaluate the global flow pattern and to validate the existence of multiple convection rolls at the chosen geometry. The latter one is believed to be a necessary condition for dust devils to emerge. The disadvantage of this set-up is that we can detect only vortices with diameters of about 50 cm or larger. This is far beyond those ones, Giersch and Raasch (2021) reported from their DNS. As a consequence, we reduced the field of view of the optical measurement (see below for a detailed description) to a volume of about 4.8 m^3 which increased the resolution of the measurement and enabled us to detect vortices down to about 1 dm size. In order to increase the probability of the occurrence of dust devil-like vortices, we placed an additional heating foil of 480 mm by 580 mm at the center of the heating plate. Similar as in nature, this generates a local hotspot with a typical over temperature of about $\Delta T_{hs} \approx 17$°C with respect to the temperature of the heating plate and may help to produce a larger number of vortices compared to the uniformly heated bottom plate.

Table 1
Summary of Experimental Parameters in This Study

Set-up	V_{opt} m^3	f Hz	T_c °C	T_h °C	ΔT_{hs} °C	Ra 10^{10}	Nu -	n m^{-3}
I.HS	43.7	10	20	30	15	1.26	145.68	12.6
I.noHS	43.7	10	15	25	-	1.37	145.68	12.3
II.HS	4.8	20	15	35	17	2.53	175.73	406.4
II.noHS	4.9	20	15	35	-	2.53	175.73	181.2

Note. Experiments set-up.I.HS, set-up.I.noHS, set-up.II.HS and set-up.II.noHS were conducted with and without additional hotspot heating (HS) in set-up I and set-up II, respectively. V_{opt} is the optical domain size (compare Figure 3) and f the recording rate. T_c, T_h, and ΔT_{hs} refer to the temperature of the top cooling plate, bottom heating plate and the temperature offset of the hotspot heating, respectively. n is the seeding particle density.

2.2. Instrumentation

2.2.1. Particle Tracking Velocimetry

Particle tracking velocimetry (PTV) is an optical flow measurement technique (Dabiri & Pecora, 2020). The fluid flow is seeded with particles which are illuminated by a light source. The light backscattered from the particles is detected using a single (planar PTV) or multiple (3-D PTV) cameras. The vectors of velocity and acceleration of the particles are identified from their displacement over a distinct time interval. Since each particle is tracked individually with time, the Lagrangian velocity field of the flow is obtained. The

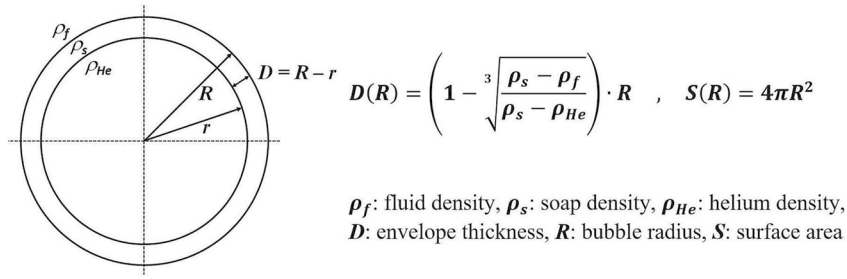

Figure 2. Soap bubble—definition of envelope thickness and surface area.

spatial resolution depends on the density of particles in the measurement volume. On the other side, the number of particles cannot be arbitrarily increased, because they must be identified one-to-one in successive recordings. For a volumetric flow measurement, multiple cameras are used to reconstruct the 3-D particle position for each recording. A synchronization between the cameras as well as with the light source is required.

2.2.2. Tracers

Particle based flow measurement technique essentially requires tracer particles that virtually follow the motion of the surrounding fluid slip-free. Moreover, the particles should feature the same density as the surrounding fluid, because otherwise, they will exhibit an artificial velocity component with or against the vector of gravity. For our experiments, they also have to be sufficiently large to be captured by the cameras at each position in the flow field. Typically used Di-Ethyl-Hexyl-Sebacat (DEHS) droplets for particle image velocimetry are not appropriate, since the particle diameter is of the order of only 1 µm (Raffel et al., 2018). However, our optical set-up requires particles with a diameter of at least a few millimeters to get detected by the cameras even at a distance of about 7 m. Here, helium filled soap bubbles turned out as ideal candidates (Loesch & du Puits, 2021). The helium applies the necessary buoyancy to the heavier soap bubble envelope and equilibrates the bubble density to the density of the surrounding air. Bubble size and envelope thickness D are linearly correlated (compare Figure 2) if density of tracers and fluid are considered equal. Since the surface area S of the bubble grows with the square of the radius R (compare Figure 2), the evaporation rate of the soap liquid grows in the same manner. This decreases the lifetime/stability of the soap bubbles when their radius increases. If considering linear correlation between surface area and evaporation rate, envelope thickness decreases transiently faster due to evaporation compared to the initial growth due to bubble size.

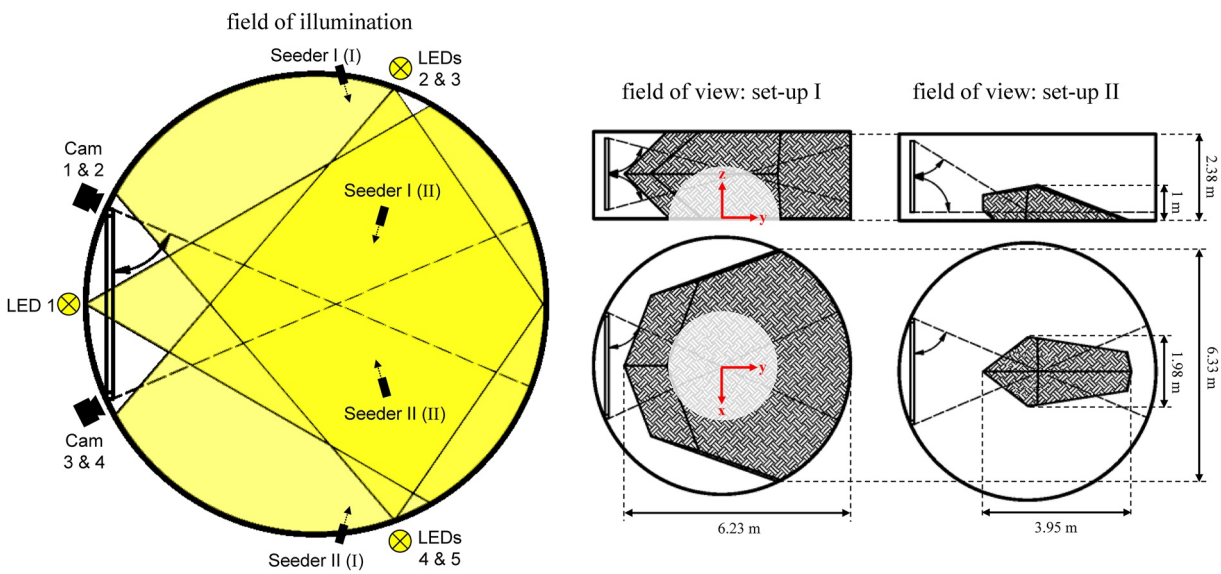

Figure 3. Field of illumination and fields of view for both set-ups with large (43.7 m^3) and reduced (4.8 m^3) optical domain. The field of illumination also depicts the position of cameras as well as the positions of the seeding generators for set-up I and set-up II and their seeding direction.

Thus, tracers should be as small as possible for elongated lifetime, but sufficiently large to be detectable by the cameras.

A dimensionless number that describes the ability of a particle to follow the motion of a surrounding fluid is the Stokes number *St*. It is defined as the ratio of relaxation time t_r of the particle and the characteristic time scale of the flow. For the following analysis, we use the free-fall time t_f which is a characteristic time scale for fast dynamics of thermal plumes and vortices in turbulent RBC (Pandey et al., 2018). These quantities are defined as follows:

$$St = \frac{t_r}{t_f} \qquad t_r = \frac{\rho_p d_p^2}{18\nu} \qquad t_f = \sqrt{\frac{L}{g\beta\Delta T}} \tag{6}$$

with ρ_p and d_p being the particle density and diameter. Three domains for the Stokes number can be determined.

- $St \ll 1$: particles follow the continuous phase of the flow
- $St \approx 1$: strong interaction between particle and continuous phase
- $St \gg 1$: particles detach the continuous phase of the flow

In our experiments the Stokes number of the helium filled soap bubbles amounts to $St \approx 0.01\ldots0.04$ which means the bubbles almost perfectly follow the large-scale pattern of fluid flow. Besides their ability to follow the flow, the soap bubbles should be neutrally buoyant. This happens due to a natural selection process. Bubbles lighter than the surrounding air will quickly move upwards, hit the cold plate and burst. Heavier bubbles will fall down, hit the hot plate and burst. Eventually, only the neutrally buoyant bubbles will remain in the fluid flow. Another buoyancy effect may occur by a possible temperature difference between the air in the Rayleigh-Bénard cell and the injected particles, which require some time to converge. The Biot number measures how fast the tracer adapts the temperature of the surrounding fluid:

$$Bi = \frac{\alpha \cdot l_c}{\lambda} \qquad l_c = \frac{r}{3} \tag{7}$$

with α, λ, and l_c being the convective heat transfer coefficient between bubble and fluid, the heat conduction coefficient of the sphere and the characteristic length, respectively. The variable r is the radius of the bubble.

At typical room temperature, values of $\alpha_{\text{air}} = 10$ W/(m^{2}K), $\lambda_{\text{He}} = 0.15$ W/(m^{2}K) and a radius of $r = 2.5$ mm result in a small Biot number of 0.06, and confirms that the thermal equilibrium between the helium in the bubble and surrounding air is achieved almost immediately and such kind of thermal buoyancy effects may be neglected. The thermal resistance of the soap envelope is very low and can be neglected therefore.

The diameter of the bubbles was chosen to be about 5 mm for those measurements covering the entire volume of the convection cell. In case of the higher resolved measurements with a reduced field of view, the diameter was reduced to about 3 mm, which led to longer lived tracers and higher particle density. The achieved particle density, resulting in active tracks in our experiments, was about 12 m^{-3}. Assuming a roughly homogeneous distribution of the tracks in space, this is a sufficient number to investigate the global flow or local coherent flow structures of larger decimeter scale. In the higher resolved experiments, the overall highest density was about 406 m^{-3} (set-up.II.HS) and 181 m^{-3} (set-up.II.noHS), which allowed the detection of smaller structures on a lower decimeter scale. This is of the order of the largest, but still also of the rarest dust devil-like vortices obtained in the numerical simulations by Giersch and Raasch (2021). However, due to the much longer observation time in our experiments, we could detect and characterize as well a reasonable number of such vortices.

2.2.3. Camera Set-Ups, Calibration, and Measurement Procedure

For all measurements, we used four cameras GO-5000M-USB (JAI Technology Co., Ltd.) with a resolution of 2560 by 2048 pixels to record the particle motion. The cameras were either equipped with 8.5 mm lenses LM8XC (KOWA optronics Co., Ltd.) to capture the entire volume of the convection cell or with 25 mm lenses LM25XC for the reduced field of view. Illumination of the particles was applied with five high power LEDs (Luxeon) fixed at the wall. One LED was placed at the center between the cameras and the other four at the sidewall of the experiment, perpendicular to the optical axis of the camera system, left and right, each two. The field of illumination and fields of view are depicted in Figure 3. The cameras and LEDs were synchronized and work with a repetition rate of 10 Hz in set-up I and 20 Hz in set-up II. The recording time for a single run was about 2 hr and limited by

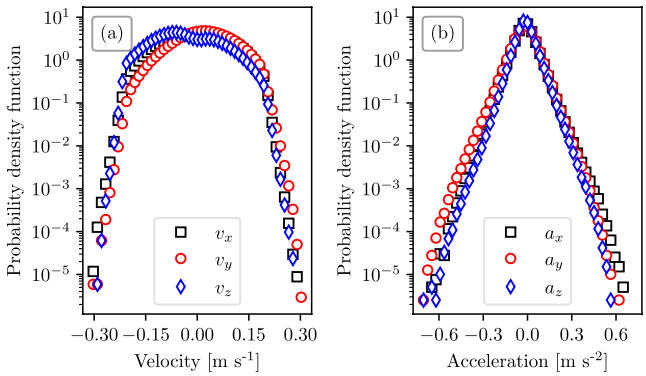

Figure 4. Probability density functions (PDF) of (a) velocity and (b) acceleration on a long period of about 5,200 s.

the capacity of the data storage system (1 hour for the reduced field of view). In order to assign the "world (3D)" coordinates to the coordinates of the four camera images, a calibration is required. This calibration was performed using a custom-made 2D calibration plate of 1,000 mm × 800 mm for the large-scale measurement, set-up I. It was consecutively placed at 30 random positions spanning the entire field of view in this set-up. We took multiple images with each of the cameras and used the mean of these images to reassign "world (3-D)" to "image (2-D)" coordinates. The algorithm used for this procedure is based on the pinhole model and solves a system of nonlinear equations. In order to increase the accuracy of the calibration, we applied a subsequent volume self-calibration algorithm (Wieneke, 2018). This algorithm uses the acquired particle images for the triangulation of real particles in the flow and refines the calibration parameters of the cameras (position, inclination, rotation, focal length of the lenses). For set-up II with the reduced field of view, we used a higher resolving 2-D calibration plate which has been imaged in three equidistant parallel positions along the optical axis. The calibration plate covers nearly the entire field of view in this set-up and a polynomial mapping could be used for calibration. It was also followed by the volume self-calibration algorithm. The soap bubbles, we used to make the air flow in the test section "visible", were injected using two particle generators. In order to obtain a maximum of bubbles in the field of view, the seeders were located in a height of about 1 m above the heating plate. They were aligned as shown in Figure 3. The seeding generators ran continuously over the entire duration of the measurement. In order to prevent any significant disturbance of the flow, we took care to keep a sufficiently large distance toward the field of view. The camera images were processed with commercial software package DaVis. Particle tracks were reconstructed using the Shake-the-Box algorithm (Schanz et al., 2016). Further data analysis, that is, vortex detection and analysis as well as the statistics of detected vortices, proceeded using in-house Python code. The Python code is available under Kaestner et al. (2023a). More details on the experimental set-up and the measurement procedure can be found elsewhere (Loesch & du Puits, 2020, 2021).

2.3. Validation of Experiment

Before we started the experiments to generate dust devil-like vortices, we have validated the measurement set-up. An appropriate method to do this is comparing the probability density functions (PDFs) of the single components of the measured velocity field. Since, we consider a turbulent flow in a closed container and the measured Lagrangian field spans almost the complete volume of the convection cell, the PDFs of the velocity and the acceleration should be symmetric about zero. We also wish to note here that only the flow field in the turbulent and well-mixed bulk is considered for this analysis. The boundary layers close to the walls are too small and cannot be resolved. A typical deviation from symmetry that may occur is a velocity or acceleration offset induced by the particle injection, that is, the airflow of the particle generator causes an artificial momentum. This artificial momentum can occur if the degree of turbulence is large and the applied momentum is low. We analyzed the measured Lagrangian fields and checked, whether the velocity of particles was homogeneously distributed in the volume. On shorter periods, local and transient events with large coherence may lead to stronger deviation of the PDFs, but will diminish on longer periods. Figure 4 shows the PDFs of velocity and acceleration components on a long period of about 5,200 s in the large volume (set-up I). The mostly symmetric distribution of all PDFs confirms a homogeneously distributed particle velocity, acceleration, and density, respectively.

2.4. Detection and Analysis of Dust Devil-Like Vortices

Detection of dust devil-like vortices directly from the Lagrangian velocity field is quite hard since particle tracks are spaced very unevenly, and moreover, they are broken very frequently. Thus, we have developed a two-step detection algorithm. It is based on transformation of the Lagrangian velocity field to a grid-based Eulerian velocity field and a subsequent algorithm to identify those vortices with a pressure drop in their center. In the first step, the Eulerian velocity field was reconstructed by binning the particle tracks to a regular grid spacing of $50 \times 50 \times 50$ mm^3 using quadratic polynoms. Then, the velocity field was checked for the existence of a vortical flow field in a 7×7 matrix around every grid point in each horizontal plane. Those grid points fulfilling this

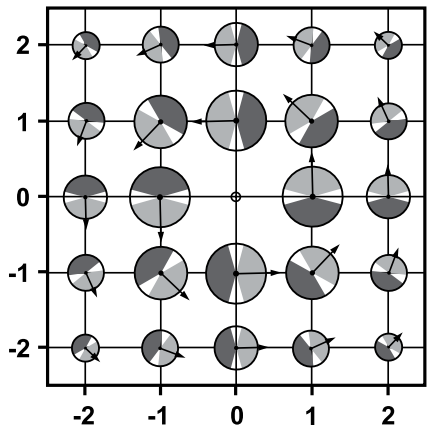

Figure 5. Detection scheme of vortices. The size of circles represents the weighting of the velocity vectors to the detection algorithm. Light and dark gray sections represent the angle of acceptance (140°) in positive and negative sense of rotation, respectively.

criterion were selected as potential candidates for a dust devil-like vortex. In the second step, the Eulerian velocity field is refined by a so-called fine-scale reconstruction algorithm (Jeon et al., 2018). The algorithm reconstructs the Eulerian field using DNS of the Navier-Stokes and continuity equations with boundary conditions (velocity and acceleration) taken from the Lagrangian field and under conservation of vorticity. This procedure provides along with the velocity field also the pressure field and enables us to apply the pressure criterion for the detection of dust devil-like vortices, according to the scheme introduced by Raasch and Franke (2011). Having found the candidates of dust devil-like vortices, we characterize their size, lifetime (observation period in set-up II), and frequency of occurrence. Unfortunately, we cannot provide the real lifetime of the structures in set-up II since they stay only a limited time in the observation area. Some of them already exist before they enter the observation area, some others still exist after leaving it. The quantities characterizing the dust devil-like vortices are defined by the following conventions: time averaged values $\bar{\cdot}$, maximum values $\hat{\cdot}$ and tangentially to the vortex center averaged values $\{\cdot\}$.

2.4.1. Detection Scheme

The detection of dust devil-like vortices was carried out by taking horizontal planes from the Eulerian field and analyzing the in-plane u and v velocity components. To this aim, the sign of each velocity component surrounding a grid point and the relative angle of the velocity vectors compared to the grid point were analyzed. Figure 5 depicts the detection scheme of vortices. If velocity vectors surrounding an individual grid point fulfill the criteria of direction within an allowed angle of acceptance of 140 grad, as shown in Figure 5, a vortex is expected. In contrast to the detection scheme of Holmén (2012), the sign is not given by the sign of the vector, but its direction. This means, vectors showing in the direction of light gray angle of acceptance receive a negative sign, and vectors showing in the direction of dark gray angle of acceptance receive a positive sign. Each surrounding vector fulfilling the individual criterion of proposed direction at the individual grid point receives a weighted value (the weight—Gaussian distribution—is visualized by the size of the circles in Figure 5). For a perfect vortex, those weighted values sum up to ± 1. Missing vectors, that is, vectors failing the allowed angle of acceptance and vectors showing in wrong direction reduce the sum from ± 1 toward zero. Thus, a new grid with probability values between ± 1 is obtained. Since the data is not perfect due to scatter in the particle tracks or errors caused by the binning process or missing vectors, values of ± 1 cannot be reached practically, and a threshold for vortex center points was set to ± 0.7. This scheme is scanned through each horizontal plane with a window size of 7×7 grid points and corresponding coordinates of vortex center grid points are captured. The combination of vortex center coordinates and the vortex rotational direction of the different planes reveals vertically connected vortices if the coordinates are close to each other and the rotational directions are the same. Last step is the logical connection of vortex cores for consecutive time steps to vortex tracks. Therefore, the vortices of the consecutive time steps have to be located in a region of acceptance which depends on the number of time steps. Five time steps in forward direction are analyzed for each time step. The allowed distance of acceptance was 2, 3, 4, 5, 5 voxels for the five consecutive time steps. If this criterion is fulfilled, two consecutive time steps were connected. This scheme was repeated for the next time step, the after next one, and so on, till the end of the measurement time. Finally, vortex tracks with lifetimes above 1.5 s were selected. They were considered to be valid by assuming this time for one complete rotation as the lower limit for a dust devil-like vortex. The selected vortices were visually verified by overlaying the vortex tracks with the circular truncated particle field around the vortex center.

Once a successive vortex track was localized in space and time, the analysis area of exactly this domain was applied for the fine-scale reconstruction. Limiting the analysis area reduces the computational time to a greatest possible degree.

2.4.2. Fine-Scale Reconstruction

The fine-scale reconstruction algorithm is based on VIC# (Vortex in Cell "Sharp"; Jeon et al., 2018). Laws of fluid dynamics are used to fill the gaps between particle tracks, deriving velocity $\mathbf{u}$, acceleration $\mathbf{a}$, and pressure p on a dense grid from particle track data by an optimization method. It calculates flow field variables by minimizing

a certain cost function J that includes several terms from two different groups. In the first group, the terms are related to the measured particle tracks, while in the second one, the terms are related to the laws of fluid dynamics and vector calculus.

The first group incorporates the measured velocities $\mathbf{u}_{\mathrm{PTV}}$ and accelerations $\mathbf{a}_{\mathrm{PTV}}$ for all N particles observed in one time step:

$$J_{\mathbf{u}} = \sum_{N} \|\mathbf{u}_N - \mathbf{u}_{PTV,N}\|^2 \tag{8}$$

$$J_{\mathbf{a}} = \sum_{N} \|\mathbf{a}_N - \mathbf{a}_{PTV,N}\|^2 \tag{9}$$

The velocity vector $\mathbf{u}$ and the acceleration vector $\mathbf{a}$ need to be known at the particle positions, but the position in the Lagrangian flow field does generally not coincide with the regularly and finitely spaced grid of the equivalent Eulerian flow field. Therefore $\mathbf{u}$ and $\mathbf{a}$ are interpolated by tri-cubic interpolation.

The second group assures the additional constraints like zero-divergence of the vorticity field j_{ω}, zero-divergence of the velocity field $j_{\mathbf{u}}$, zero-divergence of the partial derivative of the velocity field $j_{\partial u/\partial t}$, zero-rotation of the material acceleration field $j_{\mathbf{a}}$ and pressure from incompressible, inviscid Navier-Stokes equation j_p for all grid points Ω of the entire volume:

$$j_{\omega} = \sum_{\Omega} \|\nabla \cdot \omega\|^2 \tag{10}$$

$$j_{\mathbf{u}} = \sum_{\Omega} \|\nabla \cdot \mathbf{u}\|^2 \tag{11}$$

$$j_{\partial u/\partial t} = \sum_{\Omega} \|\nabla \cdot \frac{\partial \mathbf{u}}{\partial t}\|^2 \tag{12}$$

$$j_{\mathbf{a}} = \sum_{\Omega} \|\nabla \times \mathbf{a}\|^2 \tag{13}$$

$$j_p = \sum_{\Omega} \|\frac{1}{\rho}\nabla p + \mathbf{a}\|^2 \tag{14}$$

All terms sum up to the final cost function J:

$$J = J_{\mathbf{u}} + \alpha^2 J_{\mathbf{a}} + \gamma\left(h^2 j_{\omega} + j_{\mathbf{u}} + \alpha^2\left(j_{\partial u/\partial t} + j_{\mathbf{a}} + j_p\right)\right), \tag{15}$$

where h is the grid spacing, and α and γ are weighting coefficients. α is defined as the ratio of standard deviation of velocity $\sigma_{\mathbf{u},\mathrm{PTV}}$ and standard deviation of acceleration $\sigma_{\mathbf{a},\mathrm{PTV}}$:

$$\alpha = \frac{\sigma_{\mathbf{u},PTV}}{\sigma_{\mathbf{a},PTV}}. \tag{16}$$

γ is defined as:

$$\gamma = 8h^2 \frac{N_{pt}}{N_{gp}}, \tag{17}$$

where N_{pt} is the number of particle tracks and N_{gp} is the number of grid points.

2.5. Summary of Experimental Parameters

Table 1 summarizes all experimental settings we applied during our measurements. The aspect ratio and Prandtl number were fixed at $\Gamma = 3$ and $Pr = 0.71$, respectively, for all experiments. The physical domain size was always the entire volume of the test section $V = 95.6\ \mathrm{m}^3$, only the optical domain size V_{opt} was varied between set-up I and set-up II. Due to the fact that the Reynolds and Nusselt numbers were neither measured nor simulated specifically for these experiments, we have incorporated numerical values from other sources. The Reynolds

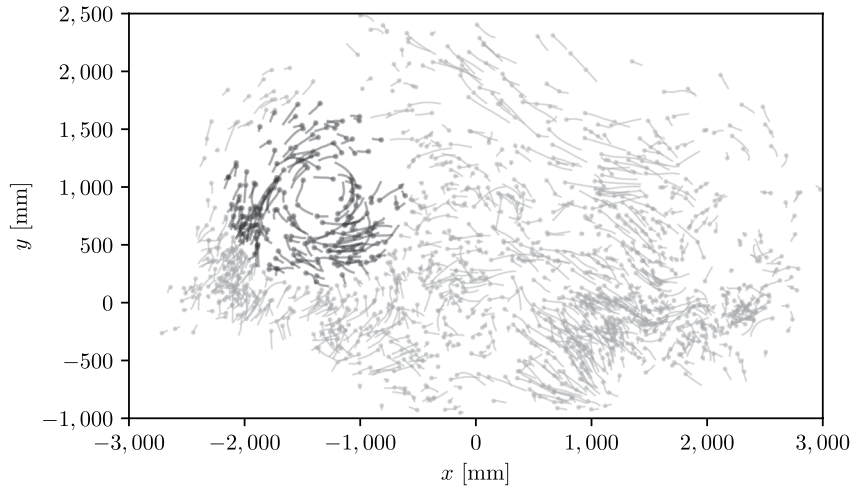

Figure 6. Large dust devil-like vortex detected in set-up.I.noHS at "Barrel of Ilmenau" after 5,007 s measurement period. Projection of the 3-D trajectories in a horizontal plane. The dust devil-like vortex (black trajectories) is emphasized.

number was roughly estimated from Du Puits et al. (2009) with $\overline{v}_{\max} = 0.33$ m/s under the assumption of a typical dimension of one half of the thickness of the fluid layer $\delta_\Theta = L/2 = 1.19$ m:

$$Re_\Theta = \overline{v}_{\max}\delta_\Theta/\nu \approx 2.5 \cdot 10^4 \tag{18}$$

This value is roughly valid for all experiments in this study. We have chosen $\delta_\Theta = L/2$ since half height of the convection cell is the equivalent of the atmospheric boundary layer.

The Nusselt number for $\Gamma = 3$ was calculated by a scaling law obtained from DNS (Bailon-Cuba et al., 2010):

$$Nu = 0.118 \cdot Ra^{0.305} \tag{19}$$

3. Results and Discussion

First, we wish to present dust devil-like vortices we could observe during the large-scale measurement setup.I.noHS (see Figure 3). These vortices were visually detected following the Lagrangian trajectories of the soap bubbles by eye and looking for circular streamlines. However, we could detect only two such structures in 20 hr measurement period, whose diameter were of the order of about 800 mm. Interestingly, both structures appeared in a short interval of about 120 s at the same position. Both vortices originated at the heating plate and extended to half height of the convection cell. This happens due to the decrease in temperature with height of the RBC which is one of the distinguishing facts with respect to the convective atmospheric boundary layer. The symmetry of RBC also may trigger dust devil-like vortices to start at the cooling plate and to extend in direction of the gravity vector to maximum half height of the convection cell. Figure 6 shows one of these two dust devil-like vortices whose lifetime amounted to about 18 s. Unlike expected, both vortices did not migrate along a path, but they only tumbled around a fixed position. For more detailed information, we refer to Kaestner and du Puits (2022). We attribute this particular behavior to the comparatively small volume of our RB cell, whose diameter is only nine times the diameter of the vortex.

Unfortunately, it was not possible to detect smaller dust devil-like structures in this set-up, since the particle density and the optical resolution of the cameras were too small. Therefore, we decided to reduce our measurement volume to about 4.9 m^3 (compare set-up II in Figure 3) which enhanced the optical resolution in the measurement volume. Moreover, we could inject the soap bubbles in a more targeted manner which increased the seeding density. This modification enabled us to detect dust devil-like vortices down to 1 dm size and raised the detection rate from two dust devil-like vortices within 20 hr measurement time to 56 vortices within 2 hr (22 vortices for set-up.II.noHS and 34 vortices for set-up.II.HS). The following discussion is, thus, solely based on the measurements using set-up II.

First of all, the properties of the detected dust devil-like vortices will be described in detail using an explicit example. This vortex, we call it the "primal dust devil-like vortex (PDD)", was also detected by eye. We used this

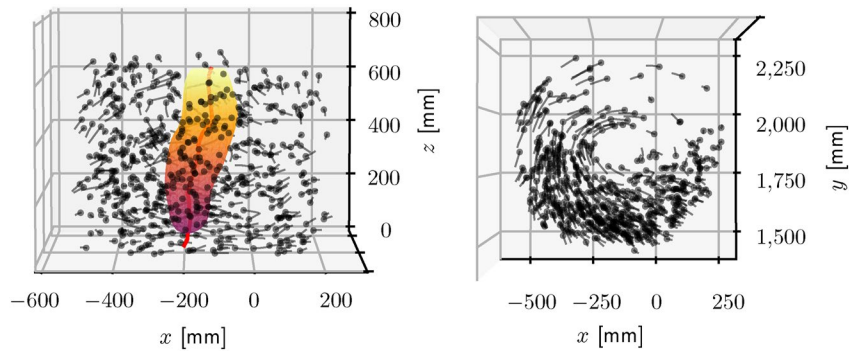

Figure 7. Lagrangian flow field and 50% isobar of maximum pressure drop of the "primal dust devil-like vortex (PDD)" measured using set-up II with the hotspot (Set-up.II.HS), right at the beginning after 11.4 s measurement period. The 50% isobar of maximum pressure drop defines the diameter of PDD. The red center line connects the points of maximum pressure drop in each horizontal grid plane of the Eulerian field. A movie of the PDD migration during the observation period can be found under Kaestner et al. (2023b).

vortex primarily to develop an algorithm to detect this kind of dust devil-like structures. PDD is also examined for its properties and compared to atmospheric dust devils. The structure could be observed over a period of about 14 s until it left the observation area. Hence it was one of the longest observed vortices in this study. Figure 7 shows the Lagrangian velocity field of PDD in side (left) and top (right) view. In order to visualize the diameter of PDD, the 50% isobar of maximum pressure drop is shown along with the particle tracks. We estimate the diameter with about 200 mm. Unfortunately, we could not determine the actual height of the vortex, since PDD spans the complete height of the observation area and may exceed it. A movie of the PDD migration during the observation period can be found under Kaestner et al. (2023b).

Figure 8 depicts a horizontal and a vertical cross-section through PDD. The horizontal cross-section is located 62 mm above the heating plate and shows the streamlines and the pressure field in the vicinity of the vortex. The characteristic pressure drop p as well as the rotational structure is visible quite well. The position of the maximum pressure drop (×) coincides with the position of the maximum vorticity, while the center of rotation of the structure (+) is about 50 mm shifted. This shift is typical for atmospheric dust devils which typically migrate along a horizontal path (S. L. Hess, 1979), compare also changes of streamlines in Harris and Durran (2006). In the flow pattern of the vertical cross-section (see Figure 8b), the typical side view of a dust devil can be seen. In the lower area ($z < 0.1$ m), air is sucked in from both sides and moves upwards in the central axis of the vortex. A few

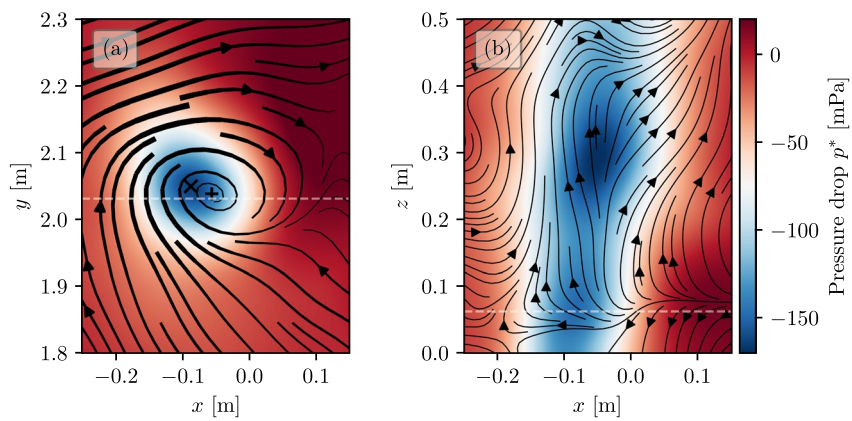

Figure 8. Streamlines and pressure field of primal dust devil-like vortex (Set-up.II.HS) in a horizontal (a) and a vertical cross-section (b). The data in the horizontal cross section was taken in a height of $z = 62$ mm, the y-position in the vertical cross-section was $y = 2.04$ m (compare the white dashed lines). The instant of time was 17.2 s (time of occurrence was 11.4–25.2 s). The thickness of streamlines in (a) represents the norm of the velocity vector. Both fields are computed using the fine-scale reconstruction algorithm of the commercial software package DaVIS. The (+) and (×) symbols mark the rotational center and the point of maximum pressure drop, respectively.

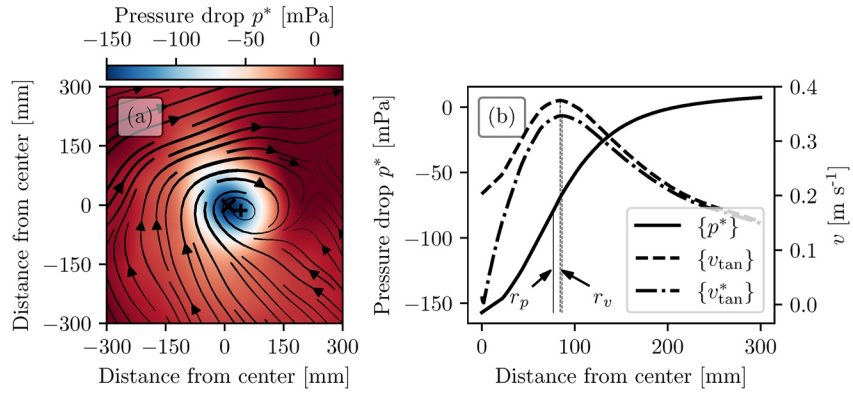

Figure 9. (a) Horizontal cross-section through primal dust devil-like vortex (Set-up.II.HS) and (b) definitions of radius, r_p and r_v, by tangentially averaged values of pressure drop $\{p^*\}$ as well as natural and corrected average tangential velocity $\{v_{\tan}\}$ and $\{v^*_{\tan}\}$, respectively. The data in the horizontal cross-section was taken in a height of $z = 62$ mm. The thickness of streamlines represents the norm of the velocity vector. The coordinates are relative to the point of maximum pressure drop.

streamlines lead directly into the bottom ($z = 0$ m), which is, presumably, an artifact of the fine-scale reconstruction algorithm. The pressure drop of about 150 mPa is of the same order of magnitude as in simulations (Giersch & Raasch, 2021), but up to four orders of magnitude smaller than for terrestrial dust devils (Metzger, 1999; Tratt et al., 2003).

The pressure and velocity fields allow the definition of the radius of the PDD (see Figure 9). For this purpose, two approaches can be found in literature. First, the radius is defined by the distance between the point of maximum pressure drop p^* (vortex center) and radius, where the pressure drop is just 50% of this maximum (Lorenz & Jackson, 2016). Second, it can be defined as the distance between the vortex center and the radius where the tangential velocity $v_{\tan}$ exhibits a maximum (Balme & Greeley, 2006). In order to simplify the comparison of various dust devil-like structures with different sense of rotation, we always count the tangential velocity as positive in the direction of rotation. We applied both methods to PDD and show the result in Figure 9. One can see that the various radii are quite similar and within the measurement and calculation uncertainties. We also applied this analysis to the tangential velocity $v^*_{\tan}$ corrected by subtracting the average migration velocity of the center, but we did not find significant impact on the result.

Next, we will discuss the lateral motion of the dust devil-like vortices which is often referred to as migration. Figure 10 depicts the migration path of the PDD (a), along with the time trace of the pressure drop $p^*(t)$ (b) as well as the migration velocity $v_{\text{migr}}(t)$ and the velocity of the background wind v_{av} (c). The background velocity v_{av} is the horizontal velocity averaged over the height of the vortex. In order to reduce the scatter of $v_{\text{migr}}(t)$ and $p^*(t)$, we smoothed both quantities migration velocity and pressure drop by a sliding average filter of 30 time steps (1.5 s) and 5 time steps (0.25 s), respectively. The intensity and direction of the background velocity fairly correspond to the migration velocity and only show low variation during the observation period. This is in agreement with atmospheric dust devils which typically move with the background wind (Reiss et al., 2016). During the observation period, the PDD covered a distance of about 2 m and achieved an average migration velocity $\overline{v}_{migr} \approx 147$ mm s^{-1}. Within this period a periodic fluctuation of the pressure drop p^* between −150 mPa and −200 mPa was observed. This is a considerably smaller pressure deficit than in atmospheric dust devils and is also well below the limit of 30 Pa to lift particles (Lorenz, 2014).

The statistical evaluation of data is, analogs to Giersch and Raasch (2021), primarily based on the maximum and minimum values of the individual parameters. Strongly fluctuating values, perhaps induced by measurement or calculation errors, were smoothed with a sliding average filter of 0.25 s before the final values of maxima or minima were identified.

Having shown horizontal and vertical slides of the instantaneous velocity and pressure fields through PDD in Figure 8, Figure 11 depicts the vertical cross-section of various parameters averaged over the entire observation period of the structures. Moreover, all structures are re-tilted from their original orientation to one perpendicular to the ground. The pressure drop of PDD (Figure 11a) has its maximum at a height of about 250 mm, and hence, above the tracing point. This is in good agreement with simulations that show the location of the

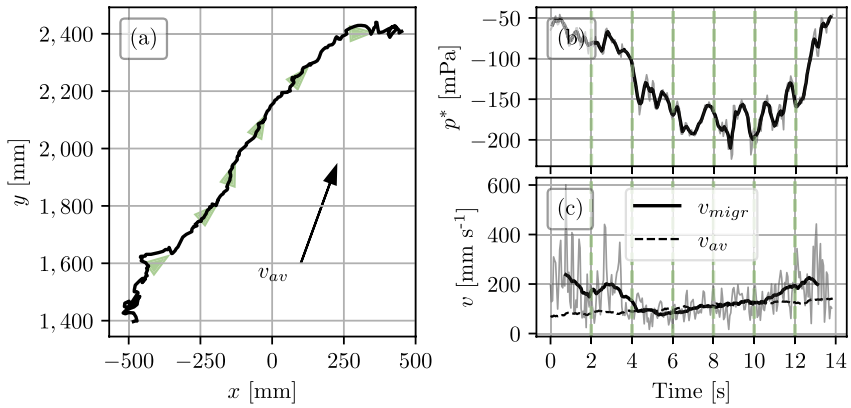

Figure 10. (a) Track of primal dust devil-like vortex (PDD; Set-up.II.HS) and prevailing background wind direction (v_{av}), (b) pressure drop p^* (raw and transiently smoothed over five time steps) and (c) migration velocity v_{migr} (raw and transiently smoothed over 30 time steps) as well as the background wind v_{av}. The green arrows in (a) mark the instants of time highlighted by the green dashed lines in (b and c). The time is relative to the start of PDD, the absolute time of occurrence was 11.4–25.2 s.

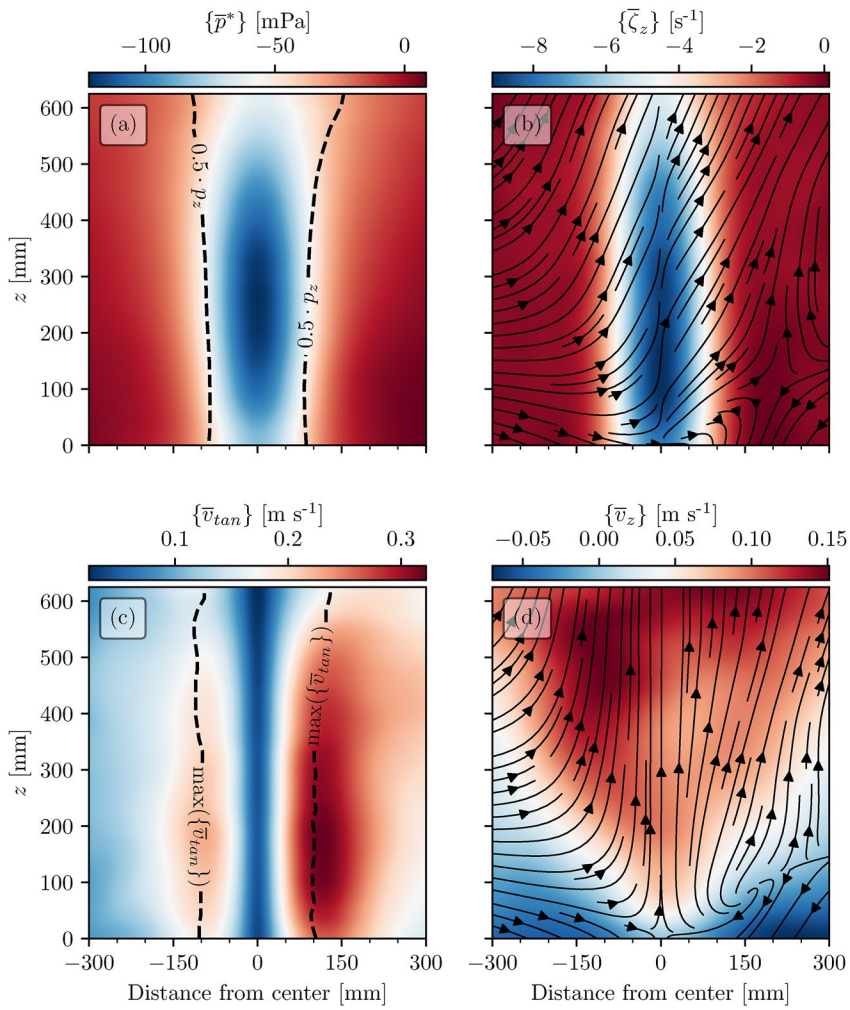

Figure 11. Pressure drop (a), vertical vorticity (b), tangential velocity (c) and vertical velocity (d) of the primal dust devil-like vortex (PDD; Set-up.II.HS). All quantities are averaged over the entire observation period. Dashed lines in (a and c) mark the diameter of PDD by the 50% pressure drop and maximum tangential velocity criterion, respectively.

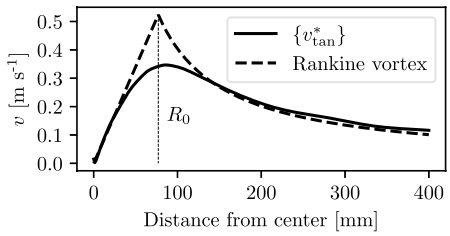

Figure 12. Comparison of the tangential velocity $\{v^*_{\tan}\}$ of primal dust devil-like vortex (Set-up.II.HS) and a Rankine vortex with $\omega = \zeta_z/2 = 3.35$ s^{-1}.

maximum pressure drop as well located somewhere above the wall (Giersch & Raasch, 2021). It is actually not clear, whether there is a correlation between the distance of the point of maximum pressure drop from the wall and the radius of dust devil-like vortices, but at least, no such correlation is known from atmospheric dust devils (Balme & Greeley, 2006). The dashed lines in Figure 11a indicate the 50% bound of the maximum pressure drop of the dust devil-like vortex and revealed a mean radius of about 100 mm. The asymmetry in the tangential velocity field (Figure 11c) shows that the dust devil-like vortex was dominantly driven from one side. The buoyancy arises from the ground over the entire observation area and is located centrally above the tracing point. A down flow in the higher center region of the dust devil-like vortex, typical for atmospheric dust devils, could not be observed. But, this might be due to the limited field of observation. The radius estimated from the tangential velocity was also about 100 mm. The dashed lines in Figure 11c mark the maximum tangential velocity as boundary of the dust devil-like vortex. The tangential velocity radially increases to a maximum and then decreases again. For the sake of completeness, also the vertical vorticity (Figure 11b) as well as the vertical velocity (Figure 11d) are shown. We wish to note here that the streamlines in Figure 11b show the natural flow field, whereas the streamlines in Figure 11d illustrate the flow field after correction by the migration velocity. The streamlines illustrate the flow field in the vertical plane. The flow pattern based on the center of rotation shows the typical flow structure of the lower part of a dust devil. Air is radially sucked in at the bottom and transported upwards. The horizontal velocity was almost zero in the vortex center. Unfortunately, we can not state anything about the upper part of the PDD since it exceeds the height of the measurement volume in this, higher resolved measurement set-up. This question has to remain open at the moment and has to be answered in future work.

Sinclair (1973) provided an interesting approach to model the tangential velocity of a dust devil and to determine its maximum pressure drop. We also tried to apply this model to the vortices observed in our experiment. Sinclair predicts the tangential velocity by a so-called Rankine vortex which is a solid-body rotation inside a cylinder of radius R_0 and a potential vortex outside the cylinder. The radius R_0 is referred to as the vortex-core radius. Figure 12 shows the radial dependence of tangential velocity of PDD in comparison with the Rankine vortex model. The tangential velocity of the Rankine vortex is determined by Equation 20. The estimate of angular velocity ω is defined by the vorticity in the vortex center $\omega = \zeta_z/2$ (Giersch & Raasch, 2021).

$$v_{\tan}(r) = \begin{cases} \omega \cdot r & \text{if } r \le R_0 \\ \dfrac{\omega R_0^2}{r} & \text{if } r > R_0 \end{cases} \tag{20}$$

The comparison shows a good agreement between the measured tangential velocity (solid line) and the velocity predicted by the Rankine vortex model (dashed line). The overestimation in the range of the vortex radius R_0 is a typical property of this model (Sinclair, 1973). This result is also in good agreement with the simulation of Giersch and Raasch (2021). The pressure drop according to the Rankine vortex p^*_R can be calculated using Equation 21 with density of air $\varrho = 1.169$ kg m^{-3} (Giersch & Raasch, 2021; Stephan et al., 2019).

$$p^*_R = \rho \cdot \omega^2 \cdot R_0^2 \tag{21}$$

The so estimated pressure drop of PDD is $p^*_R = 297$ mPa. It is about twice the pressure drop obtained from fine-scale reconstruction of $p^* = 155$ mPa. But, considering the simplicity of the Rankine vortex model and the potential uncertainties of the fine-scale reconstruction, the deviation is fairly small.

After definition of all parameters and the comparison of the "primal dust devil-like vortex" PDD with atmospheric dust devils, the following part of the paper will give an overview about the statistics of all dust devil-like vortices observed during our measurements. We start with a collection of all tracks of dust devil-like vortices in the measurement volume which is shown in Figure 13. While Figure 13a summarizes the tracks from the experiment with the overheated area at the center of the heating plate, Figure 13b shows the tracks from the experiment without this. On a first glance, it seems that the hotspot heating enhances the probability of occurrence. But, on closer examination of the experimental conditions, there is no clear correspondence. Comparing simply the number of occurring vortices per time unit, it is indeed lower in the experiment without hotspot heating (18.3

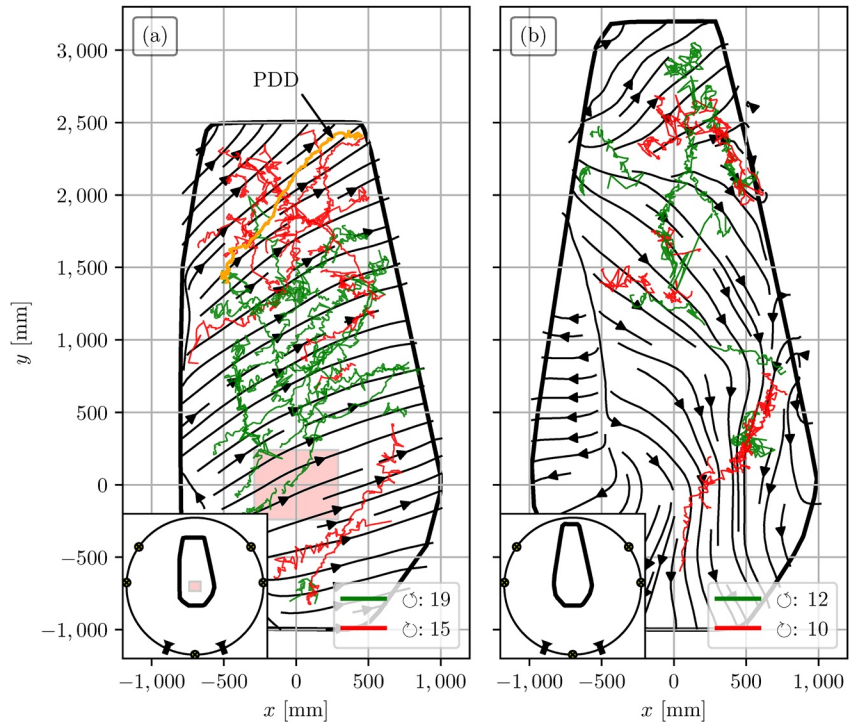

Figure 13. Overview of the tracks of all detected dust devils, (a) with and (b) without hotspot heating. Vortices with positive (green tracks) and negative (red tracks) sense of rotation as well as the observation area (black frame) are shown. The red square in (a) represents the hotspot heating mat. The streamlines illustrate the horizontal velocity field averaged over the complete measurement period in time and over the vertical extent of the measurement volume. The track of primal dust devil-like vortex (PDD) is emphasized in orange.

per hr) than in the experiment with it (43.5 per hr). However, the particle density differed from experiment to experiment which also had an impact on the volume self-calibration algorithm and hence the evaluable observation volume since the measurement field is only a fraction of about 5% of the total volume of the RB cell, and the particle concentration in the measurement volume varies as well over the time of one measurement as also from one to another measurement. As higher the particle concentration, as better the tracking algorithm works. This leads to an almost doubling of the track rate from typically about 1,000 simultaneous tracks in the experiment without hotspot heating to about 1,900 in the experiment with hotspot heating. Insofar, the difference might be rather due to the higher detection probability than to a higher rate of occurrence of dust devil-like vortices. It is also seen in the two figures that the majority of the tracks is located in the back third of the observation area and not nearby the hotspot heating, which is another indication that the hotspot may have only a minor effect on the generation of vortices. Furthermore, the streamlines in Figure 13, representing the horizontal velocity field averaged in time and over the vertical extent of the measurement volume, give no identification that the hotspot has any effect on the flow field or even the global flow has an impact on the location where the dust devil-like vortices evolve.

Table 2 summarizes the experimental results. A total of 31 vortices with positive sense of rotation and 25 vortices with negative sense of rotation were detected in both experiments. There is no preferred direction of rotation. This is in agreement with atmospheric dust devils which, in general, do not show any preference in their sense of rotation (Sinclair, 1965). We also compared the specific properties of our experimentally generated dust devil-like vortices with real dust devils. Overall, all properties of experimental vortices were orders of magnitude smaller in comparison to atmospheric dust devils. This was due to the comparably small test volume and the significantly lower Rayleigh number of the experiment, that is, $Ra \approx 10^{10}$, compared to the Rayleigh number in the convective boundary layer of the atmosphere which is about $Ra = 10^{18}$ (Giersch & Raasch, 2021).

Next, we have calculated correlations between various properties, and indeed, such correlations similar to atmospheric dust devils exist. Balme et al. (2012) showed for example, that atmospheric dust devils exhibit correlations between the maximum buoyancy velocity $\widehat{v}_z$, the radius r and the maximum migration velocity $\widehat{v}_h$. In Figure 14,

Table 2
Summary of Dust Devil Properties

Exp	N	Stats	τ s	r mm	$\{\widehat{v}_{migr}\}$ cm s^{-1}	$\{\widehat{v}^*_{\tan}\}$ cm s^{-1}	$\{\widehat{v}^*_{rad}\}$ cm s^{-1}	$\{\widehat{v}_z\}$ cm s^{-1}	$\lvert\widehat{p}^*\rvert$ mPa	$\lvert\widehat{\zeta}_z\rvert$ s^{-1}
	34	Avg	7.64	132.92	11.67	31.21	8.75	26.36	122.99	13.19
II	↻19	Std	±3.93	±50.00	±4.00	±5.52	±2.24	±7.83	±41.80	±1.78
HS	↻15	Max	14.95	244.97	21.97	40.90	13.79	46.54	214.68	16.30
	22	Avg	5.18	129.77	10.66	34.47	9.12	26.16	143.08	13.70
II	↻12	Std	±2.90	±38.04	±4.09	±5.88	±2.52	±8.47	±43.77	±1.85
noHS	↻10	Max	12.25	184.22	20.51	44.81	13.89	53.34	221.45	17.03
	56	Avg	6.67	131.68	11.28	32.49	8.89	26.28	130.88	13.39
Sum	↻31	Std	±3.74	±45.33	±4.03	±5.84	±2.34	±8.01	±43.34	±1.81
	↻25	Max	14.95	244.97	21.97	44.81	13.89	53.34	221.45	17.03

Note. Experiments (exp) set-up.II.HS and set-up.II.noHS were conducted with and without additional hotspot heating, respectively. Statistical values (stats) are given by average (avg), standard deviation (std), and maximum (max).

a correlation matrix of our data is plotted. Each diagram represents a plot of one property against one other and we used these diagrams to determine the strength of the relationship between these two properties. If a regression line can be drawn through the point cloud, a correlation exists. It is positive for a rising and negative for a falling line. In further analysis, more sophisticated functions can be used to describe the potential relations between the characteristics, but actually our data set is too small for such an analysis. Anyhow, the closer the pairs of variables are located nearby the regression function as stronger they are correlated. Correlations are moderate for values near 0.5 and strong for values of 0.9 or greater (Nachtigall & Wirtz, 2004). In contrast, homogeneously scattered

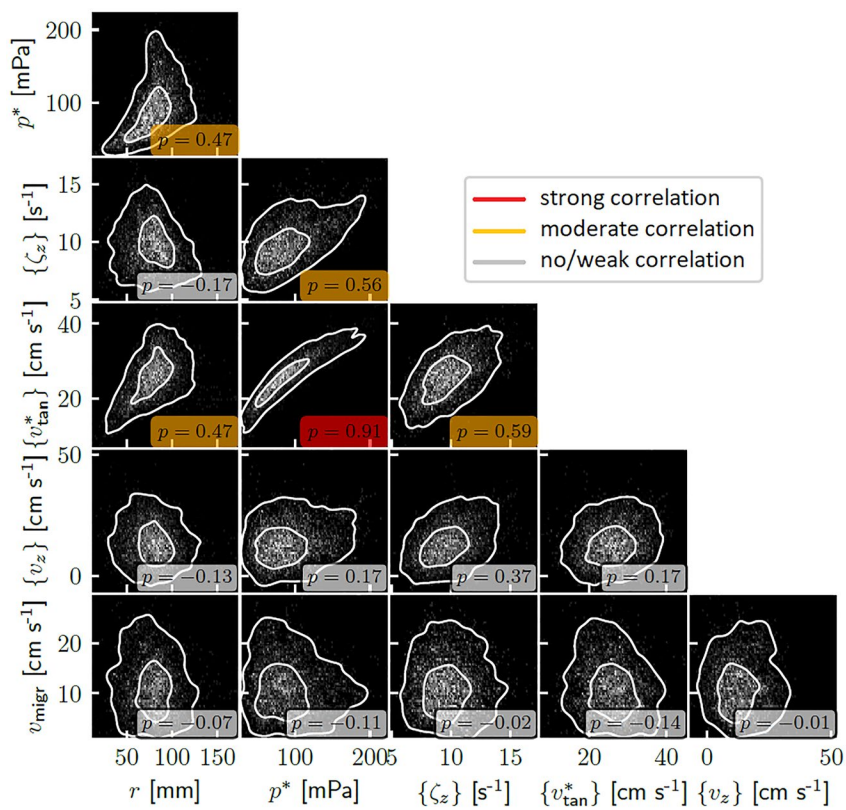

Figure 14. Correlation matrix of all extracted parameters. The inner and outer white line enclose data points within 33% and 66% of probability density, respectively.

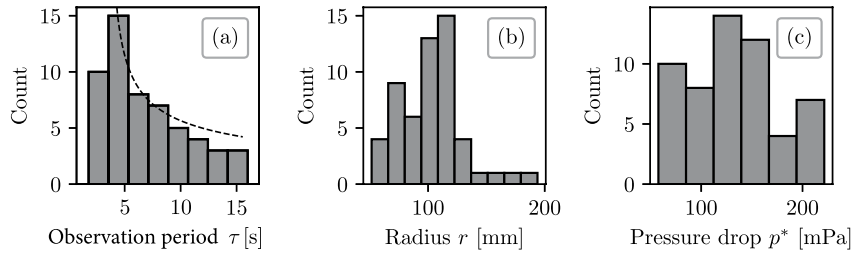

Figure 15. Histograms of observation period (a), radius (b) and pressure drop (c) of all detected dust devil-like vortices and comparison of the observation period distribution to a power law fit.

data points indicate no correlation. A strong correlation between pressure drop p^* and tangential velocity v^*_{tan} could be identified. A power law fit with $f(x) = a \cdot x^b$ reveals an exponent of $b = 1.88$ which is close to the square relationship assumed for the model of the Rankine vortex. Moderate correlations could be identified for the pairs of pressure drop and radius, vertical vorticity and pressure drop, tangential velocity and radius as well as tangential velocity and vertical vorticity. No or only very weak correlations could be found for the remaining variable pairs. In summary, we could demonstrate with our experimental work that at least a qualitative similarity to the relationships of dust devil-like vortices in DNS, but also atmospheric dust devil properties exists.

Eventually, we wish to discuss the histograms of observation period, radius and pressure drop for a statistical overview. They are shown in Figure 15. Since many of the observed vortices migrate out of the observation volume, we are not able to determine the real lifetime, and thus, we replace it by the observation period τ. The number and position of bins were defined by the Freedman-Diaconis rule (Freedman & Diaconis, 1981). The histogram of observation period also contains a power law fit to the probability density data. This is in agreement with simulations of dust devils which have also shown a lifetime distribution decreasing with a power law. The fit matches the bars in the histogram quite well for lifetimes beyond about 3 s. Interestingly, the frequency of very short-living structures is rather low which is a phenomenon that also appears in the simulations by Giersch et al. (2019). We associate this phenomenon in our experiment with the decreasing detection probability of such very short-living vortices due to the finite density of particles in the observation volume. Sinclair (1969) showed that the majority of dust devils had both shorter duration and smaller diameter. Therefore, the data was fitted by minimizing the L2 norm to the frequency data. The power law fit of the probability density distribution is given by Equation 22.

$$p_l(x) = b \cdot (x - c)^a = 0.14 \cdot (x - 3.55)^{-0.47} \tag{22}$$

The radius r and the pressure drop p^* are further dust devil properties, whose probability/frequency of occurrence is assumed to follow a power law (Lorenz, 2012). Our data does not confirm this. This is mainly due to the small number of vortices we could analyze in total. Furthermore, the probability of detection rapidly decreases for vortices with a diameter less than about 100 mm. Figure 15b shows that the frequency goes down for all radii $r < 115$ mm, although we would expect an increase. Furthermore, the pressure drop does not show a clear relationship to its frequency (Figure 15c). And last but not least, the fine-scale reconstruction meaning the transformation of the Lagrangian to the Eulerian flow field may generate some artificial effects that may consequently have an impact on the determination of the radius and the pressure drop.

Finally, we wish to compare the experimental data with data obtained from DNS of turbulent RBC (Giersch & Raasch, 2021). In the simulation, the spatial resolution of the obtained velocity field is higher than in our measurements, and thus, much more smaller vortices could be detected. This means that the mean property of each is shifted toward these smaller vortices. Table 3 shows the simulation data of the data set RA1010A3 compared to our experimental data from set-up.II.noHS (without hotspot heating). There are mostly minor variations between experimental and numerical data, and generally, the results are comparable. The difference of τ between experiment and simulation corresponds to the difference of the detected vortex sizes, that is, larger ones live longer. Furthermore, we used, a cylindrical convection cell in the experiments with diameter and height of 7.15 and 2.38 m, respectively, while simulation was based on a square geometry with dimension of $4.224 \times 4.224 \times 1.408$ m^3. The Rayleigh numbers of experiment and simulation were quite similar and amounted to $Ra \approx 10^{10}$. Considerably more structures could be detected in the simulation, however, on a much shorter time-scale. The relationship

Table 3
Comparison of Simulation (Sim) and Experiment (Exp) Without Hotspot Heating (set-Up.II.noHS)

	N	Stats	τ s	r mm	$\{\hat{v}_{\mathrm{migr}}\}$ mm s^{-1}	$\{\hat{v}^*_{\tan}\}$ mm s^{-1}	$\{\hat{v}^*_{rad}\}$ mm s^{-1}	$\{\hat{v}_z\}$ mm s^{-1}	$\lvert\hat{p}^*\rvert$ mPa	$\lvert\hat{\zeta}_z\rvert$ s^{-1}
	865	Avg	0.82	6.47	153	328	181	135	255	310
Sim	↺434	Std	±1.21	±3.13	±67.4	±133	±77.6	±31.9	±235	±125
	↻431	Max	18.8	26.3	443	1,010	526	322	1,708	928
	22	Avg	5.18	129.77	106.6	344.7	91.2	261.6	143.08	13.70
Exp	↺12	Std	±2.90	±38.04	±40.9	±58.8	±25.2	±84.7	±43.77	±1.85
	↻10	Max	12.25	184.22	205.1	448.1	138.9	533.4	221.45	17.03

Note. Statistical values (stats) are given by average (avg), standard deviation (std), and maximum (max).

between pressure drop and observation period as well as pressure drop and vorticity were similar in both experiment and simulation, while the size of dust devils and frequency of occurrence are anti-correlated. Unlike in the simulation we observed moderate correlations between vortex radius and observation period as well as pressure drop, respectively. In summary, one can state that experiments are clearly beneficial to study the very rarely occurring larger dust devil-like structures, while simulations may visualize very small structures much better. Taken into account the slightly different data base, the agreement between the data is fairly well and deviations can be reduced in future work by improving both, the experimental basis and the numerical set-up.

4. Summary and Outlook

We could experimentally demonstrate that dust devil-like vortices spontaneously arise in turbulent RBC. To our knowledge, it was one of the first-time experimental surveys to simulate the evolution of dust devil-like vortices in a laboratory experiment which mimics the convective atmospheric boundary layer quite closely and gets by without any artificial input of rotation. In our large-scale experiment, dust devil-like vortices are measured and identified using the PTV technique. Furthermore, our experimental set-up permits measuring periods of several hours and enables us to detect vortical flow structures which are somewhat rare in experimental simulations. Within an observation period of 2 hr (this is the period whose analysis has already been finished), we could detect 56 dust devil-like vortices in total. Their properties coincide quite well with those structures identified in very recent DNSs by Giersch and Raasch (2021). As well, they show similarity to atmospheric dust devils. The size of our experimentally generated dust devil-like vortices starts at about 1 dm and ranges up to about 1 m. This is larger than in DNSs but still smaller than in the atmosphere or in large eddy simulation. One limitation of our actual experiment is the maximum number of tracers/soap bubbles per volume unit at the same time which is of the order of 1 dm^{-3}. In future experiments, this might be increased by at least one order of magnitude and would make feasible monitoring the entire volume of the "Barrel of Ilmenau" (set-up I) with the same spatial resolution as we actually could realize in the reduced measurement volume (set-up II). It would reduce the uncertainty in transformation of the Lagrangian into the Eulerian velocity field and would enable us to detect all appearing dust devil-like vortices down to the decimeter scale. This will improve and expand the statistical analysis to a broader range of structure size.

Data Availability Statement

The Python code for data evaluation, dust devil detection, and characterization is available under Kaestner et al. (2023a) [Software]. A movie of the PDD migration path can be found under Kaestner et al. (2023b) [Movie].

Acknowledgments
The authors are grateful to the German Research Foundation (Deutsche Forschungsgemeinschaft—DFG) for financial support, Grant 387703749. Sabine Scherge is acknowledged for technical assistance to run the experiments. Furthermore, the authors thank Alice Loesch for setting up the experimental testing method and gathering preliminary results. Open Access funding enabled and organized by Projekt DEAL.

References

Bailon-Cuba, J., Emran, M. S., & Schumacher, J. (2010). Aspect ratio dependence of heat transfer and large-scale flow in turbulent convection. *Journal of Fluid Mechanics*, *655*, 152–173. https://doi.org/10.1017/s0022112010000820

Balme, M., & Greeley, R. (2006). Dust devils on Earth and Mars. *Reviews of Geophysics*, *44*(3). https://doi.org/10.1029/2005RG000188

Balme, M., Greeley, R., Mickelson, B., Iversen, J., Beardmore, G., & Metzger, S. (2001). A laboratory scale vortex generator for simulation of Martian dust devils. *AGU Fall Meeting Abstracts*, *2001*, P31A–P0542.

Balme, M., Pathare, A., Metzger, S., Towner, M., Lewis, S., Spiga, A., et al. (2012). Field measurements of horizontal forward motion velocities of terrestrial dust devils: Toward a proxy for ambient winds on Mars and Earth. *Icarus*, *221*(2), 632–645. https://doi.org/10.1016/j.icarus.2012.08.021

Barcilon, A. (1967). A theoretical and experimental model for a dust devil. *Journal of the Atmospheric Sciences*, *24*(5), 453–466. https://doi.org/10.1175/1520-0469(1967)024<0453:ataemf>2.0.co;2

Bell, F. (1967). *Dust devils and aviation. Meteorol (Tech. Rep.)*. Commonwealth of Australia, Bureau of Meteorology. Note 27.

Bénard, H. (1901). Les tourbillons cellulaires dans une nappe liquide. Méthodes optiques d'observation et d'enregistrement. *Journal de Physique Théorique et Appliquée*, *10*(1), 254–266. https://doi.org/10.1051/jphystap:0190100100025400

Bluestein, H. B., Weiss, C. C., & Pazmany, A. L. (2004). Doppler radar observations of dust devils in Texas. *Monthly Weather Review*, *132*(1), 209–224. https://doi.org/10.1175/1520-0493(2004)132<0209:droodd>2.0.co;2

Brooks, H. B. (1960). Shorter contributions: Rotation of dust devils. *Journal of the Atmospheric Sciences*, *17*(1), 84–86. https://doi.org/10.1175/1520-0469(1960)017<0084:sc>2.0.co;2

Carroll, J. J., & Ryan, J. A. (1970). Atmospheric vorticity and dust devil rotation. *Journal of Geophysical Researc*h, *75*(27), 5179–5184. https://doi.org/10.1029/JC075i027p05179

Chan, P. W., & Li, Q. (2021). Observation and numerical simulation of a dust devil at the Hong Kong International Airport. *Meteorologische Zeitschrift*, *30*(6), 533–543. https://doi.org/10.1127/metz/2021/1095

Cortese, T., & Balachandar, S. (1993). Vortical nature of thermal plumes in turbulent convection. *Physics of Fluids A: Fluid Dynamics*, *5*(12), 3226–3232. https://doi.org/10.1063/1.858679

Dabiri, D., & Pecora, C. (2020). *Particle tracking velocimetry*. IOP Publishing Bristol.

Du Puits, R., Resagk, C., & Thess, A. (2009). Structure of viscous boundary layers in turbulent Rayleigh-Bénard convection. *Physical Review E*, *80*(3), 036318. https://doi.org/10.1103/physreve.80.036318

Du Puits, R., Resagk, C., & Thess, A. (2013). Thermal boundary layers in turbulent Rayleigh-Bénard convection at aspect ratios between 1 and 9. *New Journal of Physics*, *15*(1), 013040. https://doi.org/10.1088/1367-2630/15/1/013040

du Puits, R., Resagk, C., Tilgner, A., Busse, F. H., & Thess, A. (2007). Structure of thermal boundary layers in turbulent Rayleigh-Bénard convection. *Journal of Fluid Mechanics*, *572*, 231–254. https://doi.org/10.1017/s0022112006003569

Fiedler, B. H., & Kanak, K. M. (2001). Rayleigh-Bénard convection as a tool for studying dust devils. *Atmospheric Science Letters*, *2*(1–4), 104–113. https://doi.org/10.1006/asle.2001.0043

Fitzjarrald, D. (1973). A laboratory simulation of convective vortices. *Journal of the Atmospheric Sciences*, *30*(5), 894–902. https://doi.org/10.1175/1520-0469(1973)030<0894:alsocv>2.0.co;2

Flower, W. D. (1936). *Sand devils*. HM Stationery Office.

Fodor, K., Mellado, J. P., & Wilczek, M. (2019). On the role of large-scale updrafts and downdrafts in deviations from Monin-Obukhov similarity theory in free convection. *Boundary-Layer Meteorology*, *172*(3), 371–396. https://doi.org/10.1007/s10546-019-00454-3

Freedman, D., & Diaconis, P. (1981). On the histogram as a density estimator: L_2 theory. *Zeitschrift für Wahrscheinlichkeitstheorie und Verwandte Gebiete*, *57*(4), 453–476. https://doi.org/10.1007/bf01025868

Giersch, S., Brast, M., Hoffmann, F., & Raasch, S. (2019). Toward large-eddy simulations of dust devils of observed intensity: Effects of grid spacing, background wind, and surface heterogeneities. *Journal of Geophysical Research: Atmospheres*, *124*(14), 7697–7718. https://doi.org/10.1029/2019jd030513

Giersch, S., & Raasch, S. (2021). Evolution and features of dust devil-like vortices in turbulent Rayleigh-Bénard convection—A numerical study using direct numerical simulation. *Journal of Geophysical Research: Atmospheres*, *126*(7), e2020JD034334. https://doi.org/10.1029/2020jd034334

Greeley, R., Balme, M. R., Iversen, J. D., Metzger, S., Mickelson, R., Phoreman, J., & White, B. (2003). Martian dust devils: Laboratory simulations of particle threshold. *Journal of Geophysical Research: Planets*, *108*(E5), 5041. https://doi.org/10.1029/2002je001987

Harris, L., & Durran, D. (2006). Streamlines versus trajectories in a translating Rankine vortex. Retrieved from https://atmos.washington.edu/durrand/animations/vort505/vortanim1.html

Hess, G. D., & Spillane, K. T. (1990). Characteristics of dust devils in Australia. *Journal of Applied Meteorology and Climatology*, *29*(6), 498–507. https://doi.org/10.1175/1520-0450(1990)029<0498:coddia>2.0.co;2

Hess, S. L. (1979). *Introduction to theoretical meteorology*. Krieger Publishing Company.

Holmén, V. (2012). Methods for vortex identification, (Master's theses in mathematical sciences).

Idso, S. B. (1974). Tornado or dust devil: The enigma of desert whirlwinds. *American Scientist*, *62*(5), 530–541.

Ives, R. L. (1947). Behavior of dust devils. *Bulletin of the American Meteorological Society*, *28*(4), 168–174. https://doi.org/10.1175/1520-0477-28.4.168

Jackson, B., Lorenz, R., Davis, K., & Lipple, B. (2018). Using an instrumented drone to probe dust devils on Oregon's Alvord Desert. *Remote Sensing*, *10*(1), 65. https://doi.org/10.3390/rs10010065

Jeon, Y., Schneiders, J., Mueller, M., Michaelis, D., & Wieneke, B. (2018). 4D flow field reconstruction from particle tracks by VIC+ with additional constraints and multigrid approximation. *Proceedings 18th International Symposium on Flow Visualization*.

Kaestner, C., & du Puits, R. (2022). Observed dust devil-like flow structures in large-scale turbulent Rayleigh-Bénard convection. *20th International Symposium on Applications of Laser and Imaging Techniques to Fluid Mechanics 2022* (pp. 1859–1871).

Kaestner, C., Schneider, J. D., & du Puits, R. (2023a). Python scripts [Software]. https://ftp.tu-ilmenau.de/hpc-private/mb/Dust_Devil_Scripts.rar

Kaestner, C., Schneider, J. D., & du Puits, R. (2023b). Video clip of PDD [Movie]. *PDD*. Retrieved from https://ftp.tu-ilmenau.de/hpc-private/mb/Kaestner_et_al_2022_dust_devil-like_vortex_in_turbulent_Rayleigh_Benard_convection.avi

Kaimal, J., & Businger, J. (1970). Case studies of a convective plume and a dust devil. *Journal of Applied Meteorology and Climatology*, *9*(4), 612–620. https://doi.org/10.1175/1520-0450(1970)009<0612:csoacp>2.0.co;2

Kanak, K. M. (2005). Numerical simulation of dust devil-scale vortices. *Quarterly Journal of the Royal Meteorological Society*, *131*(607), 1271–1292. https://doi.org/10.1256/qj.03.172

Lienhard, I., & John, H. (2005). *A heat transfer textbook*. Phlogiston Press.

Lobutova, E., Resagk, C., & Putze, T. (2010). Investigation of large-scale circulations in room air flows using three-dimensional particle tracking velocimetry. *Building and Environment*, *45*(7), 1653–1662. https://doi.org/10.1016/j.buildenv.2010.01.016

Loesch, A., & du Puits, R. (2020). Experimental investigation of dust devil like vortices with 3-D particle tracking velocimetry. *EGU General Assembly Conference Abstracts* (p. 22451).

Loesch, A., & du Puits, R. (2021). The Barrel of Ilmenau: A large-scale convection experiment to study dust devil-like flow structures. *Meteorologische Zeitschrift*, *30*(1), 89–97. https://doi.org/10.1127/metz/2020/1046

Lorenz, R. D. (2012). Power law distribution of pressure drops in dust devils: Observation techniques and Earth-Mars comparison. *Planetary and Space Science*, *60*(1), 370–375. https://doi.org/10.1016/j.pss.2011.11.003

Lorenz, R. D. (2014). Vortex encounter rates with fixed barometer stations: Comparison with visual dust devil counts and large-eddy simulations. *Journal of the Atmospheric Sciences*, *71*(12), 4461–4472. https://doi.org/10.1175/jas-d-14-0138.1

Lorenz, R. D., & Jackson, B. K. (2016). Dust devil populations and statistics. *Space Science Reviews*, *203*(1), 277–297. https://doi.org/10.1007/s11214-016-0277-9

Lorenz, R. D., Neakrase, L. D., & Anderson, J. D. (2015). In situ measurement of dust devil activity at La Jornada Experimental Range, New Mexico, USA. *Aeolian Research*, *19*, 183–194. https://doi.org/10.1016/j.aeolia.2015.01.012

Mattsson, J. O., Nihlén, T., & Yue, W. (1993). Observations of dust devils in a semi-arid district of southern Tunisia. *Weather*, *48*(11), 359–363. https://doi.org/10.1002/j.1477-8696.1993.tb05814.x

Maxworthy, T. (1972). On the structure of concentrated, columnar vortices. *Astronautica Acta*, *17*, 363–374.

McGinnigle, J. B. (1966). Dust whirls in North-West Libya. *Weather*, 21(8), 272–276. https://doi.org/10.1002/j.1477-8696.1966.tb05204.x

Metzger, S. M. (1999). *Dust devils as aeolian transport mechanisms in southern Nevada and the Mars Pathfinder landing site (Unpublished doctoral dissertation)*. University of Nevada.

Morton, B. R. (1966). Geophysical vortices. *Progress in Aerospace Sciences*, 7, 145–194. https://doi.org/10.1016/0376-0421(66)90008-x

Mullen, J. B., & Maxworthy, T. (1977). A laboratory model of dust devil vortices. *Dynamics of Atmospheres and Oceans*, 1(3), 181–214. https://doi.org/10.1016/0377-0265(77)90006-9

Murphy, J., Steakley, K., Balme, M., Deprez, G., Esposito, F., Kahanpää, H., et al. (2016). Field measurements of terrestrial and Martian dust devils. *Space Science Reviews*, *203*(1), 39–87. https://doi.org/10.1007/s11214-016-0283-y

Nachtigall, C., & Wirtz, M. A. (2004). *Wahrscheinlichkeitsrechnung und Inferenzstatistik*. Juventa-Verlag Weinheim.

Neakrase, L. D., & Greeley, R. (2010). Dust devil sediment flux on Earth and Mars: Laboratory simulations. *Icarus*, *206*(1), 306–318. https://doi.org/10.1016/j.icarus.2009.08.028

Ohno, H., & Takemi, T. (2010). Mechanisms for intensification and maintenance of numerically simulated dust devils. *Atmospheric Science Letters*, *11*(1), 27–32. https://doi.org/10.1002/asl.249

Pandey, A., Scheel, J. D., & Schumacher, J. (2018). Turbulent superstructures in Rayleigh-Bénard convection. *Nature Communications*, *9*(1), 1–11. https://doi.org/10.1038/s41467-018-04478-0

Raasch, S., & Franke, T. (2011). Structure and formation of dust devil-like vortices in the atmospheric boundary layer: A high-resolution numerical study. *Journal of Geophysical Research: Atmospheres*, *116*(D16), D16120. https://doi.org/10.1029/2011jd016010

Raffel, M., Willert, C. E., Scarano, F., Kähler, C. J., Wereley, S. T., & Kompenhans, J. (2018). *Particle image velocimetry: A practical guide*. Springer.

Reiss, D., Fenton, L., Neakrase, L., Zimmerman, M., Statella, T., Whelley, P., et al. (2016). Dust devil tracks. *Space Science Reviews*, *203*(1), 143–181. https://doi.org/10.1007/s11214-016-0308-6

Renno, N. O., Abreu, V. J., Koch, J., Smith, P. H., Hartogensis, O. K., De Bruin, H. A. R., & Carswell, A. (2004). Matador 2002: A pilot field experiment on convective plumes and dust devils. *Journal of Geophysical Research: Planets*, *109*(E7), E07001. https://doi.org/10.1029/2003JE002219

Ringrose, T. (2005). Inside dust devils. *Astronomy and Geophysics*, *46*(5), 5–16. https://doi.org/10.1111/j.1468-4004.2005.46516.x

Schanz, D., Gesemann, S., & Schröder, A. (2016). Shake-the-box: Lagrangian particle tracking at high particle image densities. *Experiments in Fluids*, *57*(5), 1–27. https://doi.org/10.1007/s00348-016-2157-1

Sinclair, P. C. (1965). On the rotation of dust devils. *Bulletin of the American Meteorological Society*, *46*(7), 388–391. https://doi.org/10.1175/1520-0477-46.7.388

Sinclair, P. C. (1969). General characteristics of dust devils. *Journal of Applied Meteorology*, 8(1), 32–45. https://doi.org/10.1175/1520-0450(1969)008

Sinclair, P. C. (1973). The lower structure of dust devils. *Journal of the Atmospheric Sciences*, *30*(8), 1599–1619. https://doi.org/10.1175/1520-0469(1973)030⟨1599:TLSODD⟩2.0.CO;2

Sorbjan, Z. (1996). Joint effects of subgrid-scale diffusion and truncation errors in large-eddy simulations of the convective boundary layer. *Boundary-Layer Meteorology*, *79*(1), 181–189. https://doi.org/10.1007/bf00120080

Spiga, A., Barth, E., Gu, Z., Hoffmann, F., Ito, J., Jemmett-Smith, B., et al. (2016). Large-eddy simulations of dust devils and convective vortices. *Space Science Reviews*, *203*(1), 245–275. https://doi.org/10.1007/s11214-016-0284-x

Stephan, P., Kabelac, S., Kind, M., Mewes, D., Schaber, K., & Wetzel, T. (2019). *VDI-Wärmeatlas: Fachlicher Träger VDI-Gesellschaft Verfahrenstechnik und Chemieingenieurwesen*. Springer-Verlag.

Stull, R. B. (1988). *An introduction to boundary layer meteorology* (Vol. 13). Springer Science & Business Media.

Sullivan, P. P., McWilliams, J. C., & Moeng, C.-H. (1994). A subgrid-scale model for large-eddy simulation of planetary boundary-layer flows. *Boundary-Layer Meteorology*, *71*(3), 247–276. https://doi.org/10.1007/bf00713741

Thess, A., Busse, F., Du Puits, R., Resagk, C., & Tilgner, A. (2001). The Barrel of Ilmenau: A novel facility for experiments on high Rayleigh number convection. In *APS Division of Fluid Dynamics Meeting Abstracts* (Vol. 54, p. JG–013).

Tratt, D. M., Hecht, M. H., Catling, D. C., Samulon, E. C., & Smith, P. H. (2003). In situ measurement of dust devil dynamics: Toward a strategy for Mars. *Journal of Geophysical Research: Planets*, *108*(E11), 5116. https://doi.org/10.1029/2003je002161

Wieneke, B. (2018). Improvements for volume self-calibration. *Measurement Science and Technology*, *29*(8), 084002. https://doi.org/10.1088/1361-6501/aacd45

Williams, N. R. (1948). Development of dust whirls and similar small-scale vortices. *Bulletin of the American Meteorological Society*, *29*(3), 106–117. https://doi.org/10.1175/1520-0477-29.3.106

Willis, G., & Deardorff, J. (1979). Laboratory observations of turbulent penetrative-convection planforms. *Journal of Geophysical Research: Oceans*, *84*(C1), 295–302. https://doi.org/10.1029/jc084ic01p00295